Carbon Trends 25 (2026) 100698

Contents lists available at ScienceDirect

Carbon Trends

journal homepage: www.elsevier.com/locate/cartre

Ozone induced surface functionalization of hard carbon for sodium-ion batteries: Mechanism, composition, and electrochemical impact

Felix Bauer, Marius Ast, Alperen Kahraman, Frieder Scheiba *

Institute for Applied Materials, Karlsruhe Institute of Technology, Eggenstein-Leopoldshafen 76344, Germany

ARTICLE INFO

Keywords:
Sodium-ion battery
Hard carbon
Oxygen functional groups
Solid electrolyte interphase
Ozone

ABSTRACT

The potential of hard carbon as an anode material for sodium-ion batteries is well-recognized, yet its electrochemical performance remains strongly influenced by incompletely understood surface chemistry. Oxygen functional groups (OFGs) have been reported to exert both beneficial and detrimental effects on solid electrolyte interphase (SEI) formation, initial coulombic efficiency (ICE), and Na^+ transport, but their specific roles are often obscured by concurrent chemical and structural changes induced by conventional oxidation treatments. Here, ozone is investigated as a controllable gas-phase oxidant for surface functionalization of hard carbon. By varying the treatment temperature, we distinguish facile functionalization at room temperature, which predominantly targets edge and defect sites, from over-oxidation at 60–100 °C, which induces pronounced structural degradation and generation of low-molecular highly-oxidized compounds. On this basis, we propose a mechanistically inspired, ozonolysis-type framework to describe ozone-induced hard carbon functionalization and structural degradation. Electrochemically, moderate ozone functionalization improves interfacial kinetics and SEI formation without sacrificing reversible capacity, whereas excessive oxidation increases polarization and reduces the ICE. The results of this work refute the common assumption that a high surface oxygen content inherently leads to poor ICE. Instead, both ICE and reversible capacity are governed primarily by the accessibility of the internal porosity.

1. Introduction

The development of advanced energy-storage materials is critical to meet the demand for efficient and sustainable technologies [1]. Porous non-graphitizable carbons (hard carbons) have emerged as leading anode candidates for post-lithium systems, particularly sodium-ion batteries. Their disordered microstructure resists graphitization even at temperatures above 3000 °C, enabling sodium storage capacities >200 mAh g^{-1}, far exceeding graphite's theoretical limit of 35 mAh g^{-1} (NaC_{64}) [2].

The surface chemistry of hard carbon critically influences electrochemical performance because the surface directly contacts the electrolyte and mediates interfacial reactions, including electrolyte decomposition and solid electrolyte interphase (SEI) formation. Although various strategies like particle surface coating or binder induced SEI formation exist, direct modification of surface oxygen functional groups (OFGs) is a straightforward way to modify the surface chemistry [3,4]. However, oxygen functionalization of hard carbon is a double-edged sword: insufficient affinity of the OFG restricts Na^+ transport into the bulk, whereas excessive binding immobilizes ions and irreversibly consumes sodium inventory [5,6].

Despite extensive study, the role of surface OFGs in determining the initial coulombic efficiency (ICE) still remains unresolved in the literature, as OFGs have been reported to exert both positive and negative effects on the ICE (Table 1) [4,6–10]. For example, Ghimbeu *et al.* showed that nitric acid functionalization of cellulose-derived hard carbon increased oxygen content but reduced ICE from 82.7% to 55.9% [10]. Subsequent hydrogen annealing removed OFGs, yet further decreased ICE to 48.2%, demonstrating that ICE cannot be explained by OFG content alone.

Similarly, Wang et al. reported ICE values for hard carbons with comparable oxygen contents depending on the applied treatment [6]. Despite exhibiting comparable oxygen contents (20.1 and 17.6 at.%), mechanochemical CO_2 treatment and acid treatment resulted in markedly different ICE values of 47.7% and 71.4%, respectively, highlighting the importance of treatment-induced structural changes beyond oxygen functionalization alone.

Therefore, chemical functionalization is strongly coupled to

* Corresponding author.
E-mail address: frieder.scheiba@kit.edu (F. Scheiba).

https://doi.org/10.1016/j.cartre.2026.100698
Received 25 June 2026; Received in revised form 1 September 2026; Accepted 16 September 2026
Available online 17 September 2026

Table 1
Literature overview of different oxygen functionalization.

Precursor @$T_{carbonization}$	Treatment	O-content / at.%	ICE /%	Electrolyte	Reference
Glucose @900 °C	H_2SO_4 + $KMnO_4$	22.1	55	1 M $NaClO_4$ EC:PC:FEC	[7]
Potassium citrate @750 °C	HNO_3	20.2	82	1 M $NaClO_4$ EC:PC	[8]
Sucrose @800 °C	H_2O_2	10.0	20	1 M $NaClO_4$ EC:PC:FEC	[14]
Coconut shell @1300 °C	KOH	n/A	70	1 M $NaPF_6$ EC:DMC	[9]
Glucose @700 °C	Air at 700 °C	13.3	47.3	1 M $NaClO_4$ EC:DEC:FEC	[15]
Cellulose @1400 °C	$HNO_3 + H_2$	n/A	48	1 M $NaPF_6$ EC:DMC	[10]
Anthracite @1600 °C	CO_2 ball milling	5.7	33	1 M $NaClO_4$ EC:PC:FEC	[6]
Sucrose @1300 °C	HNO_3	16.0	30	0.8 M $NaPF_6$ EC:DMC	[4]
Cellulose @1000 °C	CO_2 ball milling	19.3	40	1 M $NaClO_4$ EC:DEC	[12]
Sucrose @1300 °C	O_2 plasma	15.6	66	1 M $NaClO_4$ EC:PC	[16]
Commercial HC	O_2 plasma	10.0	81	1 M $NaPF_6$ Diglyme	[17]
Litchi wood @1400	O_2 plasma	n/A	90	1 M $NaPF_6$ DEGDME	[18]
Apricot shells @900 °C	H_2 at 800 °C	4.6	73	1 M $NaClO_4$ EC DEC	[19]

concurrent structural changes, obscuring the individual contributions to the electrochemical behavior. Common strategies to modify surface oxygen content often fail to consistently discriminate between oxygen functionalization and structural effects of the treatment route [10–13]. Consequently, the mechanistic links between the surface oxygen chemistry, interfacial reactivity, and SEI evolution in sodium-ion batteries are still poorly defined.

Herein, we introduce a facile and selective surface-functionalization approach using ozone as a gaseous oxidant. With a high oxidation potential of 2.07 V (vs. SHE), ozone can readily introduce OFGs to activated carbons [20], graphene [21,22], graphite [23,24], and carbon nanotubes [25,26]. Previous studies have proposed that ozone can attack unsaturated carbon bonds, edge sites and defects, leading to the formation of epoxide, hydroxyl, and carbonyl functionalities through a Criegee-type mechanism [20,22,26–29]. Theoretical studies further support ozone-induced oxidation of sp^2-rich carbon materials *via* Criegee-type intermediates, linking the formation of oxygen functional groups to concurrent structural degradation of the carbon framework under severe oxidation conditions [30].

To the best of our knowledge, the application of ozone to hard carbon materials and its implications for electrochemical performance in sodium-ion batteries have not yet been systematically studied. We demonstrate that treatment temperature controls the balance between oxygen functionalization and structural degradation of the carbon framework. Correlation with the electrochemical behavior reveals distinct effects on ICE, ion-transport kinetics, and reversible capacity, establishing ozone treatment as a straightforward surface-engineering strategy and providing design principles for optimized hard carbon surface chemistries.

2. Experimental methods

Hard carbon (HC) was synthesized according to Yao et al. [31]. by dissolving 4.67 *g* Pluronic F127 in 187 mL ethanol and 56 mL Milli-Q water, followed by addition of 25 mL furfuryl alcohol (Sigma-Aldrich, 98%) and stirring for 15 min. Polymerization was initiated by adding 11 mL concentrated HCl and stirring overnight. Cross-linking was induced by adding 126 mL 5 M H_2SO_4 and heating to 100 °C until a brown paste formed. The paste was washed three times with Milli-Q water, purified by centrifugation, dried at 80 °C, and ground to a fine powder.

Pyrolysis was performed under argon (0.5 L min^{-1}) by heating to 200 °C (2 h) for pre-carbonization, followed by a ramp of 1 K min^{-1} to 850 °C and a 5 h dwell. After cooling, the resulting hard carbon powder was used without further purification.

Glassy carbon electrodes were obtained from redox.me, and highly ordered pyrolytic graphite (HOPG) from SPI Supplies.

2.1. Ozone treatment

For surface functionalization, 1 *g* pristine HC was finely ground, spread in an alumina crucible, and treated with ozone for 3 h. Ozone was generated using a Woodland WOZ 3 ozonator operated at full power with an oxygen flow rate of 0.5 L min^{-1}. A reference sample was treated identically at 100 °C without ozone exposure. Glassy carbon and HOPG samples were treated under identical ozonation conditions.

2.2. Electrode preparation

Electrodes were prepared by mixing 93 wt.% active material with 1.4 wt.% carbon black (TIMCAL Super C65), followed by dropwise addition of Milli-Q water and mixing in a THINKY planetary speedmixer (1500 rpm, 2 min). Subsequently, 1.87 wt% carboxymethyl cellulose (2 wt.% aqueous solution) and 3.73 wt.% styrene-butadiene rubber (39.8 wt.% aqueous solution) were added and mixed for 5 min at 800 rpm. The resulting slurry was doctor-blade coated onto aluminum foil (250 μm gap) and dried sequentially at room temperature overnight, at 80 °C for 12 h, and finally at 120 °C under vacuum overnight. Electrode active mass loading were typically ~4.5 mg cm^{-2}.

2.3. X-Ray photoelectron spectroscopy (XPS)

XPS was performed using a Thermo Scientific K-Alpha+ spectrometer with a monochromatic Al Kα X-ray source (1486.6 eV, 400 μm spot size) employing a concentric hemispherical analyzer (pass energies: 200 eV survey, 50 eV for high-resolution spectra). Samples were mounted on silicon wafers using carbon tape. The Thermo charge neutralization system was used which employed 8 eV electrons and low-energy Ar^+ ions.

Spectra were analyzed using Thermo Avantage software with Shirley background subtraction and referenced to the sp^2 C1s peak at 284.4 eV. The sp^2 asymmetry was modeled using a tail mix of 70–90%, tail exponent 0.04–0.06, and FWHM of 0.8–1.3 eV. Other C1s components (C–C/C–H, C–O, O═C–O) were fitted using mixed Gaussian–Lorentzian profiles (FWHM: 1.3–1.6 eV), and O1s components with FWHM of 1.6–2.3 eV. Elemental compositions were quantified using Scofield sensitivity factors [32]

The C KLL Auger D-parameter, defined as the energy separation between the maximum and minimum of the first derivative, was used to assess sp^2/sp^3 hybridization. KLL spectra were smoothed using a Gaussian filter (FWHM: 2 eV) and differentiated with a width of 2.10 eV.

2.4. Scanning electron microscopy (SEM)

SEM images were acquired using a thermal field-emission SEM (Carl Zeiss SMT AG) operated at 5 kV. Samples were mounted on steel holders using carbon tape.

2.5. Raman spectroscopy

Raman spectra were recorded using a LabRAM HR Evolution spectrometer (HORIBA Scientific) with a HeNe laser (632.8 nm), 600 *g* mm^{-1} grating, and 50 × objective. At least three spectra were collected per sample from different regions. Data were processed using CasaXPS with

cubic spline background subtraction. D and G bands were fitted with absolute Lorentzian profiles, while residual features were fitted using mixed Gaussian–Lorentzian functions.

2.6. Thermogravimetric analysis (TGA)

To monitor the pyrolysis procedure in hindsight to mass loss and decomposition of OFGs, thermogravimetric analysis coupled with infrared spectroscopy was carried out on a Netzsch STA 449C Jupiter and a Bruker Alpha-p Tensor II instrument equipped with an external gas flow cell analyzer.

Samples were analyzed in argon by heating from 30 °C to 1200 °C at a ramp of 5 K min^{-1}. Infrared spectra were simultaneously recorded from 700 to 3000 cm^{-1}.

2.7. Brunauer-emmett-teller surface area (BET)

N_2 adsorption isotherms were recorded at 77 K using Anton Paar Nova 800 high-vacuum physisorption analyzers. Pore size distributions were obtained from the adsorption branch by the QS-DFT method using the Kaomi software package with slit and spherical pore geometries [33].

2.8. Cell assembly

2.8.1. 3-Electrode half-cells

Electrochemical measurements were conducted in custom PEEK 3-electrode cells (Fig. S1) [34]. Cell assembly was performed in an argon-filled glovebox (MBraun) with O_2 and H_2O levels <0.1 ppm. Working electrodes (12 mm) were separated from a 12 mm sodium metal counter electrode by two glass-fiber separators (Whatman GF/D). A sodium reference electrode was positioned perpendicular to the working electrode (Fig. S1). Cells were filled with 400 µL 1 M $NaPF_6$ in EC:PC (50:50 wt.%) with 5 wt.% fluoroethylene carbonate (Sigma-Aldrich, 99%).

2.9. Electrochemical measurements

Electrochemical testing was conducted at 25 °C using a BioLogic VMP3 potentiostat. Cells were rested at open-circuit potential for 8 h prior to testing. Galvanostatic cycling was performed between 2.0 V and 5 mV vs. Na^+/Na with current densities normalized to active mass.

2.10. Rate tests

Rate performance was evaluated over five cycles at 50, 100, 200, 500, and 1000 mA g^{-1}, followed by 10 cycles at 50 mA g^{-1} to assess reversibility.

2.11. Cyclic voltammetry (CV)

Cyclic voltammetry was performed between 2.0 V and 5 mV vs. Na^+/Na at scan rates of 0.1, 0.2, 0.5, 0.7, and 1 mV s^{-1}, with five cycles per scan rate.

2.12. Potentiometric electrochemical spectroscopy (PEIS)

PEIS measurements were conducted using an 8 mm hard carbon working electrode and a 12 mm NVP/C counter electrode with Na^+/Na reference after five formation cycles at 50 mA g^{-1} and ~100% state of charge. Spectra were collected from 200 kHz to 10 mHz with a sinusoidal 10 mV perturbation and 9 points per decade.

2.13. Galvanostatic intermittent titration technique (GITT)

Sodium diffusion kinetics were evaluated by GITT using a 12 mm HC electrode vs. sodium after five formation cycles at 50 mA g^{-1}. Current pulses at 20 mA g^{-1} for 1800 s were followed by 2 h relaxation. Apparent diffusion coefficients were calculated using the Weppner–Huggins method based on the potential response during relaxation [35,36].

3. Results and discussion

Oxygen surface functionalization of hard carbon was achieved by subjecting furfuryl alcohol derived hard carbon spherules to a stream of ozone or oxygen at different temperatures. To maintain consistent nomenclature, samples are denoted as HC–X–T, where X describes the atmosphere of the treatment (O_3 or O_2) and T the treatment temperature in °C.

Scanning electron microscopy (SEM) was used to study particle size, morphology and surface texture. As shown in Fig. 1, furfuryl derived HC consists of spherical particles with an average diameter of 3.9 µm. A quantitative particle size distribution derived from SEM image analysis is provided in the Supporting Information (Fig. S2). HC–O3–25 exhibits no morphological differences compared to HC and also the average diameter is comparable. In contrast, HC–O3–60 and HC–O3–100 exhibit a smaller average diameter of 3.4 and 3.2 µm and display pronounced surface roughening, which can be attributed to the increased oxidative reactivity of ozone at elevated temperatures that leads to carbon surface erosion, which could also cause the loss of near-surface carbon mass and structural degradation [20]. This interpretation is further supported by the observed 17.8% mass loss for HC–O3–100 (Table 2). Given the open porosity of hard carbon, the observed structural degradation at elevated ozone-treatment temperatures is likely not limited to the external particle surface but also propagates into the particle. HC–O2–100 was prepared to isolate the role of ozone in the functionalization process (Fig. 1e). In comparison with the other samples, the morphology of HC–O2–100 closely resembles HC and lacks the ozone-induced surface features, confirming that ozone and not oxygen alone drives the observed morphological changes.

HC–O3–100 was immersed in water and subsequently washed by centrifugation, yielding the sample HC–O3–100W. During this procedure, the aqueous phase developed into a dark, non-sedimenting solution (Fig. S3a). After drying, the residue accounted for approximately 15% of the sample, which suggests the formation of water-soluble oxidation products during ozone treatment. SEM imaging of the dried dispersion revealed a non-conductive, brittle film (Fig. S3b). Although the exact molecular composition remains unresolved, these observations are consistent with the presence of a heterogeneous mixture of low-molecular oxidized carbonaceous fragments (LOCs). The morphology and surface texture of HC–O3–100W differ markedly from the other samples and exhibit a substantially smoother appearance, suggesting partial coverage of the particle surface by these oxidation products (Fig. S3d). Despite extensive washing, the surface layer could not be visibly removed, indicating strong interactions between the oxidized fragments and the hard carbon surface. Additional insights into the chemical composition of the LOCs is provided by XPS analysis in the following section.

The reactivity of the HC–O3–100 surface is further corroborated by observations made during electrode fabrication, as agglomeration of the slurry occurred upon the addition of the aqueous SBR-CMC binder mixture. The agglomeration can plausibly be explained by a pH shift due to potentially introduced acidic surface groups by the ozone treatment, which affect the CMC binder. On the other hand, SBR contains unsaturated double bonds that are susceptible to radical-initiated reactions, and ozone in aqueous environments can generate hydroxyl radicals (•OH) capable of attacking such moieties [37,38]. In the presence of reactive oxygen species, radical-mediated crosslinking of SBR may explain the observed agglomeration.

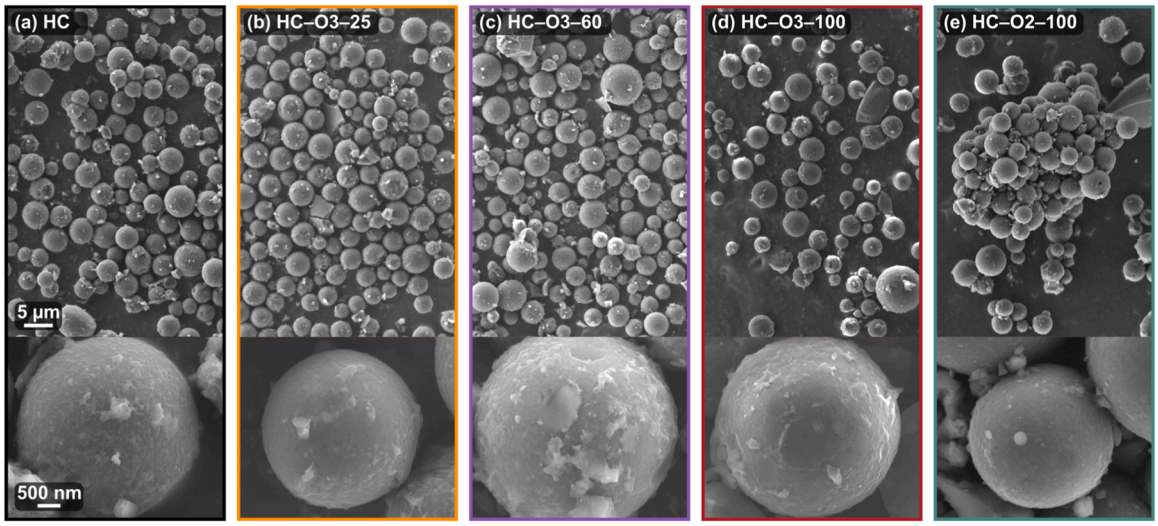

Fig. 1. SEM micrographs of pristine and treated hard carbon particles at different magnifications. a) HC. b) HC–O3–25. c) HC–O3–60. d) HC–O3–100. e) HC–O2–100.

Table 2
Residual masses and average sphere sizes of hard carbon before and after treatment.

sample	residual mass after treatment / %	Average sphere size / µm
HC	-	3.9
HC–O3–25	105.5	3.7
HC–O3–60	98.2	3.4
HC–O3–100	82.2	3.2
HC–O2–100	95.4	3.6

3.1. *Surface analysis of ozone treated hard carbons*

X-ray photoelectron spectroscopy (XPS) was employed to determine surface elemental composition and oxidation states, enabling detailed analysis of oxidation and bonding environments in hard carbon. Survey spectra (Fig. 2a) show that all samples consist predominantly of carbon and oxygen, with no significant impurities. Ozone treatment markedly increases the O 1 s signal (~530 eV): oxygen content rises from 5.9 at.% for HC to 21.0 at.% for HC–O3–25. Notably, oxygen uptake is non-monotonic with temperature, decreasing slightly from 30.5 at.% for HC–O3–60 to 27.9 at.% for HC–O3–100. The reduced oxygen content at 100 °C likely reflects the temperature-accelerated oxidation rate that promotes OFG cleavage and CO_2 release, consistent with Arrhenius-type kinetics and studies of ozone with activated carbons [20]

High-resolution C 1s spectra (Fig. 2c) of HC are dominated by an asymmetric sp [2]. C–C peak at 284.4 eV with a π–π* shake-up feature at ~290.5 eV, characteristic of graphitic domains [39]. Weak higher binding energy contributions correspond to C–O (~286.6 eV) and O═C–O (~289.0 eV) species, associated with hydroxyl/ether and carboxyl-type functionalities, respectively [40,41]. Their low intensity reflects extensive oxygen removal during pyrolysis as CO, CO_2, or small organics, with residual oxygen likely incorporated in thermally stable cyclic structures requiring >700 °C for cleavage [10,42,43]

HC–O3–25 exhibits increased C–O and O═C–O contributions, confirming effective oxidation. Additional features appear at ~288.0 eV, assigned to O–C–O and C═O species, and at ~285.0 eV, attributed to sp [3]. carbon and carbon adjacent to oxygenated sites [43]. With increasing ozone treatment temperature, oxygen-related peaks broaden and intensify, resembling a higher degree of functionalization and increased chemical heterogeneity. Simultaneously, the relative intensity of the sp^2. peak decreases, while its full width at half maximum (FWHM) expands from 1.1 to 1.3 eV, indicating increased structural disorder. The O═C–O peak at ~289.0 eV becomes the dominant oxidized-carbon feature, identifying carboxyl-type species as major oxidation products.

HC–O3–100W exhibits a slight increase in the sp^2-carbon contribution compared to HC–O3–100 (Fig. S4a), reinforcing the plausible presence of LOCs on the surface. In contrast, the intensities of oxidized-carbon spectral components (C–O, C═O, O═C–O) remain unchanged, indicating that the dominant surface functionalities persist after washing. Only O–C–O and C═O contributions decrease, suggesting that these groups undergo hydrolysis upon contact with water. Analysis of the washed supernatant confirms this interpretation: peaks and intensities in C 1s spectra closely match those of HC–O3–100, demonstrating the presence of a surface-anchored LOC layer (Fig. S4b). Although these data do not permit identification of discrete molecular species, elemental quantification of the centrifugate (Table S1) confirms the highly oxidized character of the dissolved degradation products, revealing an oxygen content of 34.8 at.% together with substantial contributions from C–O and O═C–O functionalities. The comparatively high oxygen content and the dominance of oxidized carbon species suggest that the degradation products are not highly graphitized carbon fragments but rather small and oxygen-rich structures containing a large fraction of carboxyl and hydroxyl functionalities. IR spectroscopy of the centrifugate corroborates the high concentration of oxygen functional groups in LOCs (Fig. S4 c).

O 1s spectra (Fig. 2d) offer complementary information. For comparison, spectra were deconvoluted into three components: single-bonded O–C (~533 eV), double-bonded O═C (~532 eV), and at ~535.5 eV attributed to adsorbed water [42]. Table 3 shows an increase in C═O contributions for HC–O3–25 and HC–O2–100, while C–O species slightly dominate for samples treated with ozone elevated temperatures

Surface graphitization was assessed using the C KLL Auger D-parameter, which represents the energy difference between extrema in the first derivative of the carbon KLL transition. This semi-empirical metric ranges from ~13 eV for sp^3-rich carbons to ~22.5 eV for purely sp^2. carbon [44]. HC exhibits a D-parameter of 18.1 eV, corresponding to ~34% sp^2. content typical of amorphous carbons. Regardless of treatment temperature, ozone lowers the D-parameter to 14.6–15.1 eV, indicating a surface sp^2. contribution below 10%. C KLL Auger electrons, being more surface-sensitive than C 1 s photoelectrons due to their shorter inelastic mean free paths, provide a more comprehensive understanding of depth-dependent oxidation when combined with the results from XPS [41]. HC–O3–25 has a predominantly modified outermost surface, whereas higher-temperature treatments extend

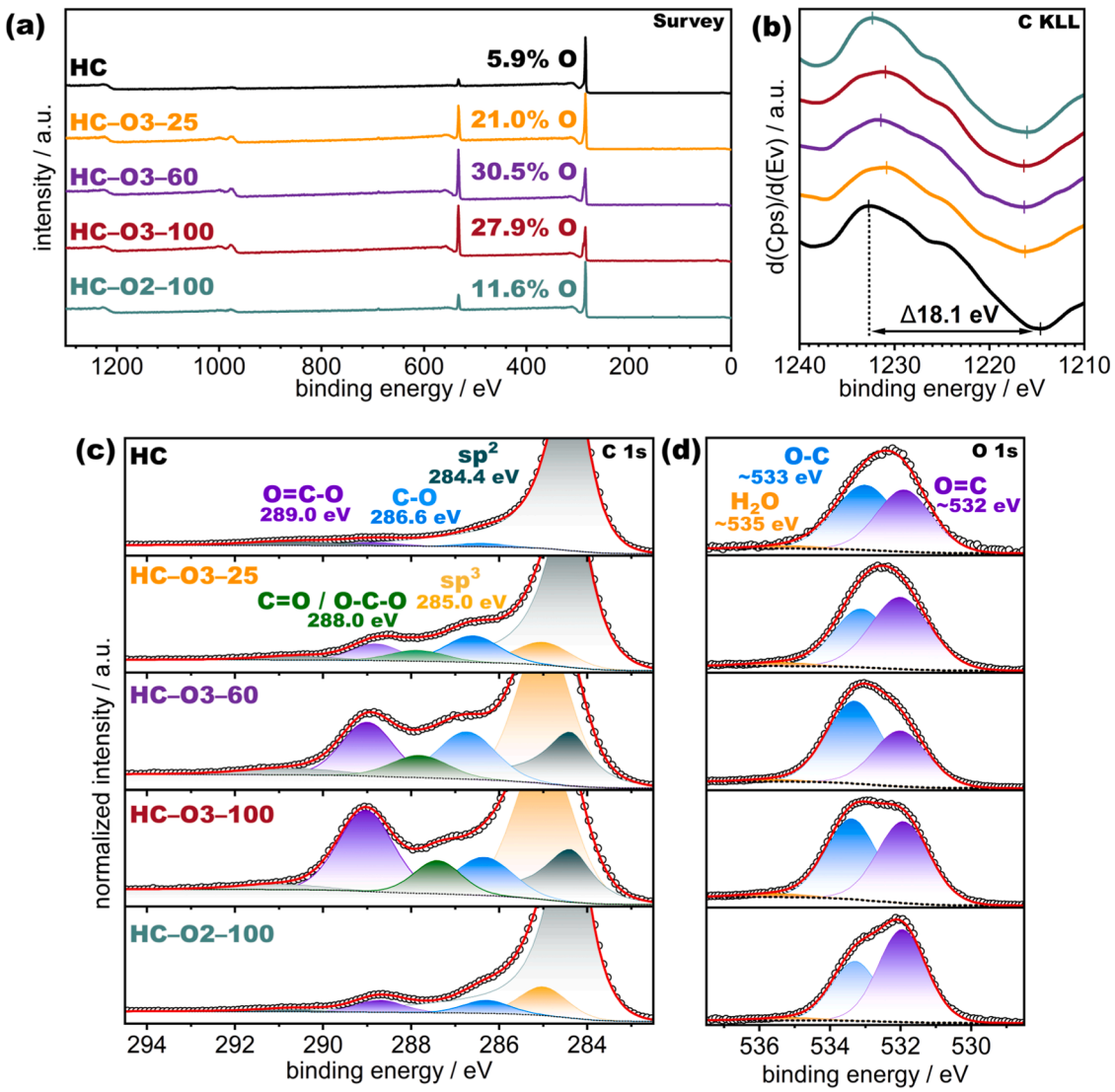

Fig. 2. XPS characterization of pristine and treated hard carbons. (a) XPS survey spectra showing the surface elemental composition. (b) First derivative of the C KLL Auger transition used for determination of the D-parameter. (c) High-resolution C 1 s spectra with deconvolution and assignment of oxygen-containing carbon species. (d) High-resolution O 1 s spectra showing the distribution of oxygen functionalities.

Table 3
XPS parameters for pristine and ozone treated hard carbon as well as the oxygen reference.

sample	overall		O1s		D-Parameter
	C /at. %	O /at. %	O-C / %	O=C /%	/eV
HC	93.3	5.9	53.3	46.7	18.1
HC–O3–25	77.4	21.0	40.5	59.5	14.6
HC–O3–60	68.0	30.5	57.5	42.5	15.1
HC–O3–100	72.0	29.0	57.1	42.9	14.6
HC–O2–100	85.5	11.6	41.4	58.6	16.3

oxidation into subsurface regions. This distinction is critical because surface OFGs directly govern SEI formation, while subsurface oxidation may promote additional irreversible capacity losses by sodium trapping.

3.1.1. *Proposed mechanism of ozone-induced functionalization*

A mechanistic model based on classical ozonolysis is proposed to rationalize the oxygen functionalities formed on hard carbon surfaces. Ozonolysis, originally described by Criegee, involves the cleavage of C═C bonds via reactive ozone intermediates and has been conceptually adapted to carbonaceous materials [27,45,20,26,22,46]

Fig. 3a summarizes the proposed reaction sequence. Ozone initially undergoes a 1,3-dipolar cycloaddition with reactive carbon edge sites (I), forming a short-lived molozonide intermediate (II) [27,47]. This concerted process involves simultaneous HOMO–LUMO interactions between the C═C bond and the ozone molecule (Fig. S5). The molozonide subsequently rearranges, cleaving a C–C bond to yield a Criegee intermediate (III), which further cyclizes into a trioxolane (IV). In the presence of water, oxygen or additional ozone, the trioxolane hydrolyzes, producing carboxylic acids, carbonyls, and hydroxyl groups (V) [27].

Correlation of this reaction sequence with XPS-derived carbon oxidation states motivates the surface-functionalization model proposed in Fig. 6. HC is dominated by sp^2. carbon (284.4 eV) with only minor oxidized contributions, consistent with an intact graphitic network. Initial ozone exposure introduces C–O bonds at edge sites, reflected by growth of the ~286.6 eV peak, while rearrangement to reactive trioxolane-type intermediates correlates with the emergence of an O–C–O feature at ~288 eV. Subsequent hydrolysis or oxidation generates carboxyl-type species, evidenced by the increasing O═C–O peak at ~289.0 eV [22].

Fig. 3b shows the proposed functionalization mechanisms for ozone

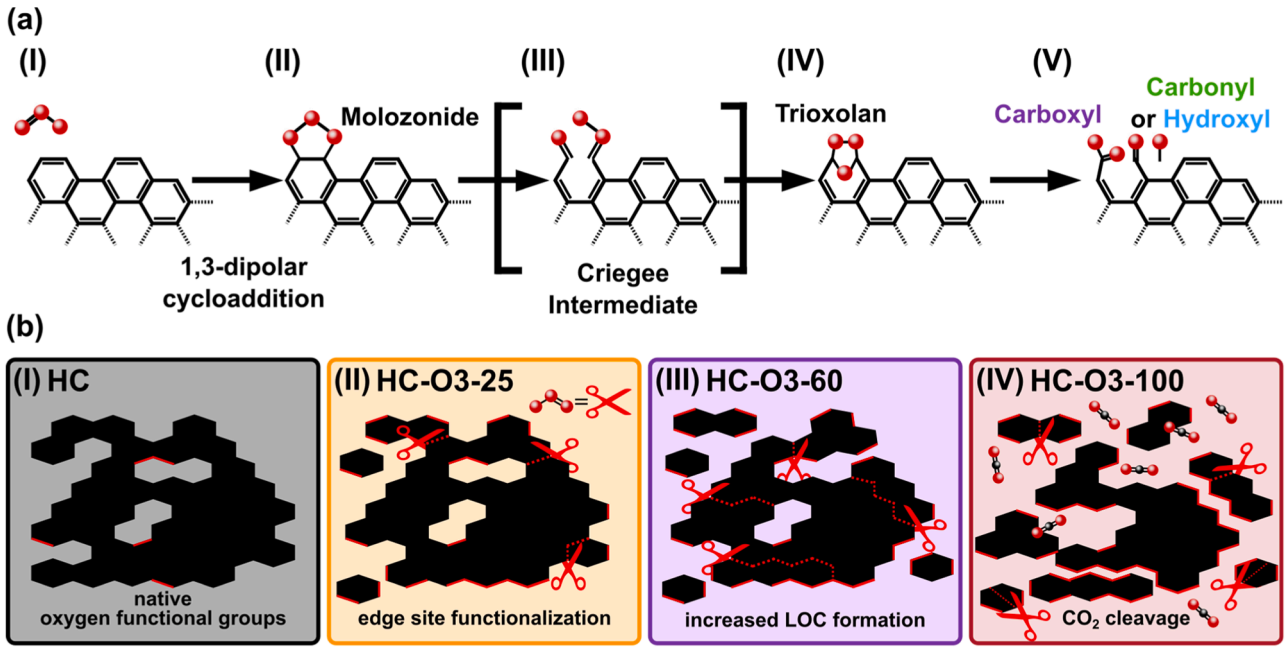

Fig. 3. a) Proposed reaction mechanism of ozone with hard carbon. b) Proposed functionalization mechanism and generation of LOCs on the hard carbon with ozone at different temperatures.

interaction with hard carbon at different temperatures. HC exhibits an intact sp^2. basal plane with only small contributions from oxygen functional groups likely located at edge sites (I). At 25 °C, reaction kinetics are slow and ozone molecules mainly functionalize edge and defect sites, which does not lead to significant LOC generation (II). Based on activation energies for oxidative and surface-bound reactions, increasing the temperature from 25 °C to 60 °C accelerates the reaction by approx. one order of magnitude, corresponding to a 10–20-fold increase in reaction rate. This accelerated reaction rate accounts for the increased LOC formation (III). Ozone molecules not only functionalize edges sites, but also act as a "molecular scissor" and excise LOCs out of the hard carbon sp^2. planes. Because ozone can diffuse through the intrinsic open porosity of HC, LOC formation is expected to occur not only at the external surface but also within the particle. However, the thermal energy at 60 °C remains insufficient to promote significant conversion of these fragments into CO_2. The highest reaction rate is thus expected for HC–O3–100 and at this temperature, it is also plausible that LOCs themselves further react to CO_2 explaining the significant mass loss observed (IV).

3.2. *Glassy carbon and highly ordered pyrolytic graphite as model substrates for ozone activation*

To further elucidate ozone reactivity and validate the proposed mechanism, glassy carbon electrodes (GCE) and highly ordered pyrolytic graphite (HOPG) were subjected to identical ozone treatments at 25 °C and 100 °C. Glassy carbon can be considered a dense form of hard carbon produced by high-temperature pyrolysis (~3000 °C) with minimal intrinsic oxygen. Both substrates confine chemical reactions to the surface, which renders them ideal models for surface functionalization with ozone [29,48]

Because sodium does not significantly insert into GCEs, the electrochemical response is dominated by surface reactions. Consistent with this, XPS depth profiling shows that oxygen signals of a pristine GCE vanish after ~60 s of Ar^+ sputtering, confirming surface-limited native oxygen functionalities (Fig. S7a). Morphological changes upon ozone treatment are temperature dependent: pristine GCE exhibits a smooth, featureless surface, while ozone at 25 °C produces only sparse shallow craters, likely at pre-existing defects. In contrast, treatment at 100 °C yields a pronounced microstructured, fractal ridge-like morphology, which aligns with our expectations for ozone-induced degradation of sp^2-carbon domains at elevated temperatures (Fig. 4a).

XPS corroborates these trends, as ozone exposure at 25 °C increases the oxygen content to ~6.8 at.% (Fig. S7b), with minimal changes in C 1s spectra but a clear rise in O–C contributions in O 1s spectra, consistent with surface-confined functionalization (Fig. 4b and c). At 100 °C, the strong morphological modification is accompanied by a high abundance of oxidized carbon species in C 1s and a pronounced O 1s signal.

HOPG was examined as a basal-plane-dominated model with minimal defect density. Freshly cleaved HOPG shows no detectable oxygen signal (Fig. S7c). Ozone treatment at 25 °C introduces a modest oxygen content (~2.5 at.%), consistent with literature, indicating limited basal-plane functionalization [29]. Given the predominance of basal-plane carbon in HOPG, edge sites contribute <1% to the XPS signal, confirming that ozone can also functionalize basal planes, albeit weakly. Treatment at 100 °C does not increase oxygen uptake (~2.1 at.%), further indicating limited basal-plane reactivity. However, mechanically roughened HOPG exposed to ozone at 100 °C exhibits substantially higher oxygen content (~4.4 at.%), demonstrating that defects and edge sites are the primary ozone-attack sites, while intact basal planes remain quasi inert to ozone erosion mechanisms [29].

3.3. *Structural and thermogravimetric characterization*

Raman spectroscopy was used to probe the degree of structural disorder in the hard carbon framework. Owing to the highly disordered nature of low-temperature pyrolyzed hard carbons, first-order Raman spectra cannot be adequately described by the D and G bands alone. Instead, the spectra were deconvoluted using a five-band model consisting of the D (~1338 cm^{-1}), D' (~1620 cm^{-1}), D" (~1500 cm^{-1}), D* (~1200 cm^{-1}), and G (~1585 cm^{-1}) contributions, which has previously been shown to provide a more appropriate description of amorphous carbon materials [49]. Because these bands are broad and strongly overlapping, intensities of the deconvoluted peaks and their integrated areas were evaluated (Table S2). The D band originates from defect-activated breathing modes of sp^2 carbon rings, while the G band corresponds to in-plane stretching of sp^2. C–C bonds in graphitic domains [50]. The peak intensity I_D/I_G and area ratios A_D/G_G are therefore

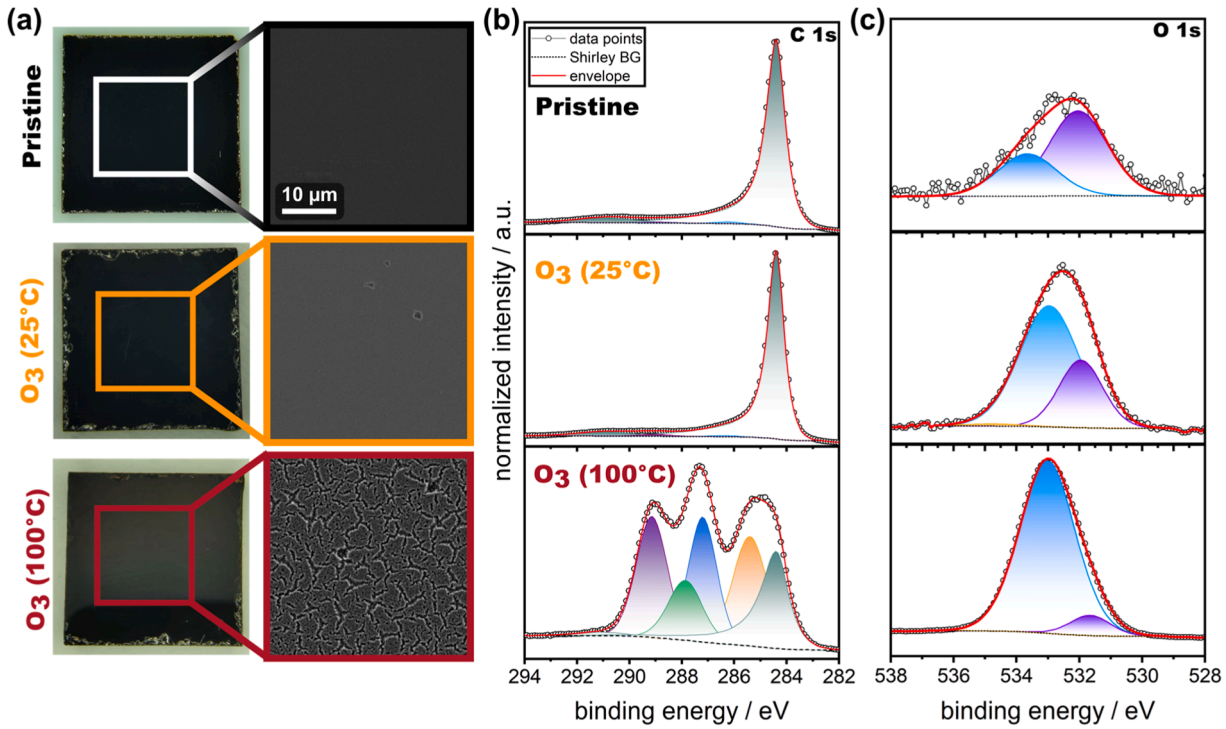

Fig. 4. Characterization of pristine and ozone-treated glassy carbon electrodes. (a) Optical microscopy and SEM images showing the surface morphology before and after ozone treatment. (b) High-resolution XPS C 1 s spectra of the corresponding glassy carbon electrodes. (c) O 1 s spectra showing the increase in oxygen-containing surface functionalities upon ozone treatment.

commonly employed as a qualitative descriptor of structural disorder in amorphous carbons. As Raman spectroscopy probes a comparatively large sampling volume (>50 nm) it is not considered surface-sensitive. The obtained spectra primarily reflect changes in the bulk carbon framework rather than the chemistry of the outermost surface.

Given the relatively low pyrolysis temperature of 850 °C, extensive graphitization in the materials is not expected. Accordingly, both pristine and ozone-treated samples are highly amorphous and defect-rich,

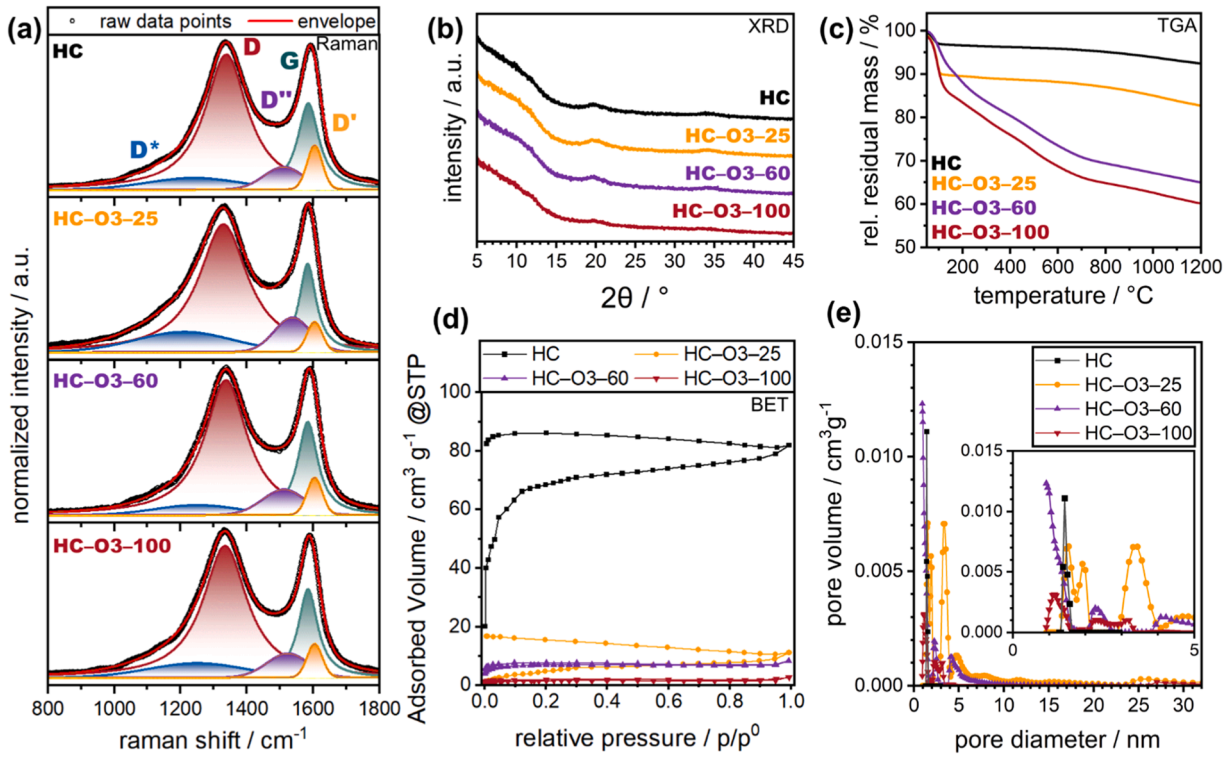

Fig. 5. Structural characterization of pristine and ozone-treated hard carbons. (a) Deconvoluted Raman spectra showing changes in structural disorder. (b) Corresponding XRD patterns. (c) Thermogravimetric mass-loss profiles. (d) N_2 adsorption isotherms measured at 77 K. (e) Pore-size distributions analysis.

as supported by X-ray diffraction patterns, which show only broad reflections (Fig. 5b). Crystallite sizes are thus expected to be very small, and the Raman response is dominated by molecular-scale structural units inherited from the precursor rather than extended graphitic domains [51]. Under these conditions, the Tuinstra–Koenig relation between A_D/A_G and lateral crystallite size (L_a) is not applicable, as it is valid only for $L_a > 2$ nm [51,52]. Moreover, the D band reflects disorder-activated lattice vibrations rather than specific defect types, and bulk disorder contributes significantly to its intensity. Consequently, Raman spectroscopy cannot identify individual oxygen functional groups or distinct defect chemistries in hard carbon [15]. Nevertheless, comparative Raman analysis provides insight into relative structural changes. Deconvoluted Raman spectra of pristine and ozone-treated samples (Fig. 5a) show broad, overlapping bands characteristic of amorphous carbons, which is consistent with previous reports on oxygen functionalized hard carbons [7,9].

3.3.1. Effects of ozone treatment on Raman features

Ozone treatment at 25 °C induces a red shift of the D band from 1338 to 1329 cm^{-1} and leads to a decrease in I_D/I_G from 1.56 to 1.44, while the relative peak area ratio A_D/A_G increases from 3.10 to 4.13 (Table 4). The divergence between intensity- and area-based disorder indicates that ozone treatment does not uniformly affect all defect environments but instead leads to a redistribution of structurally distinct defect populations within the hard carbon framework. The reduced I_D/I_G ratio suggests preferential oxidation of defective carbon regions like edge sites, which are abundant in HC and particularly susceptible to ozone attack [29]. Consequently, the data from Raman spectroscopy do not indicate a simple reduction in disorder, but rather a modification of the defect structure induced by ozone treatment, consistent with the preferential functionalization and oxidation of defect-rich and edge-site carbon environments identified by XPS. At higher treatment temperatures, I_D/I_G increases slightly, indicative of progressive carbon framework erosion that increases the relative contribution of edge sites. This interpretation aligns with SEM observations of increasingly roughened particle surfaces for hard carbon and glassy carbon samples treated at 100 °C.

Analysis of the $I_D/I_{D'}$ ratio can provide further information on the defect character. Ratios of ~3 are observed for pristine and high-temperature-treated samples, which corroborate the presence of edge-type defects, whereas higher ratios (~7) are associated with vacancy-like defects [53]. The 25 °C ozone-treated sample exhibits an increased $I_D/I_{D'}$ ratio, suggesting vacancy formation under slow reaction kinetics. At elevated temperatures, secondary oxidation of initial vacancies likely generates additional edge sites, reducing the ratio again. Interestingly, the ratio of A_D/A_{D*} exhibits a maximum for HC–O3–60. While the D* band cannot be ascribed directly to LOCs, its evolution is consistent with evolution of sp^2-sp[3]. bonding environments associated with polyene like species and coincides with the temperature regime where LOC formation is proposed to be most pronounced (HC–O3–60) [49].

3.3.2. Thermogravimetric analysis: oxygen functional group desorption

Thermogravimetric analysis (TGA) was employed to assess the thermal stability and desorption behavior of oxygen functional groups (Fig. 5d). HC shows an initial mass loss of ~4% at 100 °C due to desorption of adsorbed moisture, followed by a near constant mass up to ~800 °C and a gradual decline at higher temperatures, consistent with desorption of residual oxygen functionalities.

Oxygen functional groups decompose over characteristic temperature ranges: aldehydes/ketones (200–400 °C, CO), carboxylic acids/anhydrides (400–650 °C, CO_2), ethers/phenols (600–800 °C, CO), quinones/carbonyls (750–1000 °C, CO_2), and cyclic species such as lactones or pyrans (600–800 °C, CO_2) [54,55]. Because pyrolysis of the hard carbon precursor was performed at 850 °C, the remaining mass loss above 850 °C is attributed primarily to decomposition of residual thermally stable cyclic oxygen groups.

HC–O3–25 exhibits a TGA profile similar to the pristine material but with pronounced mass loss at 100 °C, ascribed to increased surface polarity and moisture uptake. In contrast, HC–O3–60 and HC–O3–100 show substantially different profiles, which are consistent with previous reports on ozone treated activated carbons [20]. The pronounced additional mass loss below ~800 °C is ascribed to the decomposition of the proposed LOC species. This interpretation is further supported by in-line recorded IR measurements, which reveal increasingly pronounced CO_2 evolution for HC–O3–60 and HC–O3–100 compared to pristine HC (Fig. S8). Notably, the additional CO_2 release occurs predominantly between approximately 200 and 800 °C, coinciding with the temperature range in which the ozone-treated samples exhibit the strongest excess mass loss relative to pristine HC. Above ~800 °C, the mass-loss profiles become nearly parallel, indicating that the additional mass loss is largely associated with the decomposition of ozone-induced oxidation products. The increased CO_2 evolution therefore corresponds with the thermal decomposition of highly oxidized carbonaceous degradation products generated during ozone treatment. Residual masses of ~65% (HC–O3–60) and ~60% (HC–O3–100) support the removal of LOCs during heating. Given the ~30 at.% oxygen content determined by XPS, the observed mass losses are quantitatively reasonable.

Table 4
Parameters for Raman spectroscopy and thermogravimetric analysis.

sample	Raman spectroscopy					BET surface area	TGA residual mass
	I_D/I_G	A_D/A_G	$I_D/I_{D'}$	$A_D/A_{D'}$	A_{D*}/A_D	m^2	wt.%
HC	1.56	3.10	3.04	12.05	7.46	220	92
HC–O3–25	1.44	4.13	4.21	19.23	4.5	20.0	83
HC–O3–60	1.45	3.08	3.59	14.08	9.62	21.5	65
HC–O3–100	1.49	3.38	3.88	15.87	5.85	5.0	60

3.4. Electrochemical characterization

3.4.1. Cyclic voltammetry

Cyclic voltammetry (CV) was employed to correlate oxygen functionalization with the electrochemical response of ozone-treated hard carbon and model carbon substrates, providing insights into potential-dependent electrolyte decomposition, SEI formation, and sodium-storage processes during initial cycling.

Fig. 6a–d shows the first five CV cycles of pristine and ozone-treated hardcarbon electrodes at 0.1 mV s^{-1}. HC exhibits a cathodic onset near ~1 V vs. Na^+/Na, commonly attributed to sodium adsorption at defect sites and oxygen functional groups [6]. Given the low oxygen content of HC (5.9 at.%), the density of reactive SEI-forming sites is limited. The redox peak at 0.1 V reflects sodium insertion and pore filling, while the reverse scan shows a broad anodic feature corresponding to sodium extraction [9,56]. The progressive increase of the peak-current over successive cycles indicates gradual accessibility of pore storage sites, whereas strong overlap of CV curves between 0.1 and 1.0 V demonstrates high reversibility in the sloping-potential region. The first-cycle charge consumption of HC–O3–25 is reduced, indicating suppressed irreversible reactions, while higher insertion currents imply facilitated interfacial kinetics despite increased OFG density as confirmed by XPS. This behavior is consistent with formation of a more ion-conductive SEI and enhanced charge-transfer kinetics promoted by surface functionalization, particularly at edge or defect sites [6,12].

In contrast, HC–O3–60 shows strongly diminished insertion currents in the first cycle and negligible activity in subsequent cycles (Fig. 6c), indicating the suppression of reversible sodium storage at low potentials. A reason for this suppressed insertion is the presence of LOCs inside the particle, which block the internal porosity being responsible for the storage of sodium at low potentials. HC–O3–100 exhibits a broad

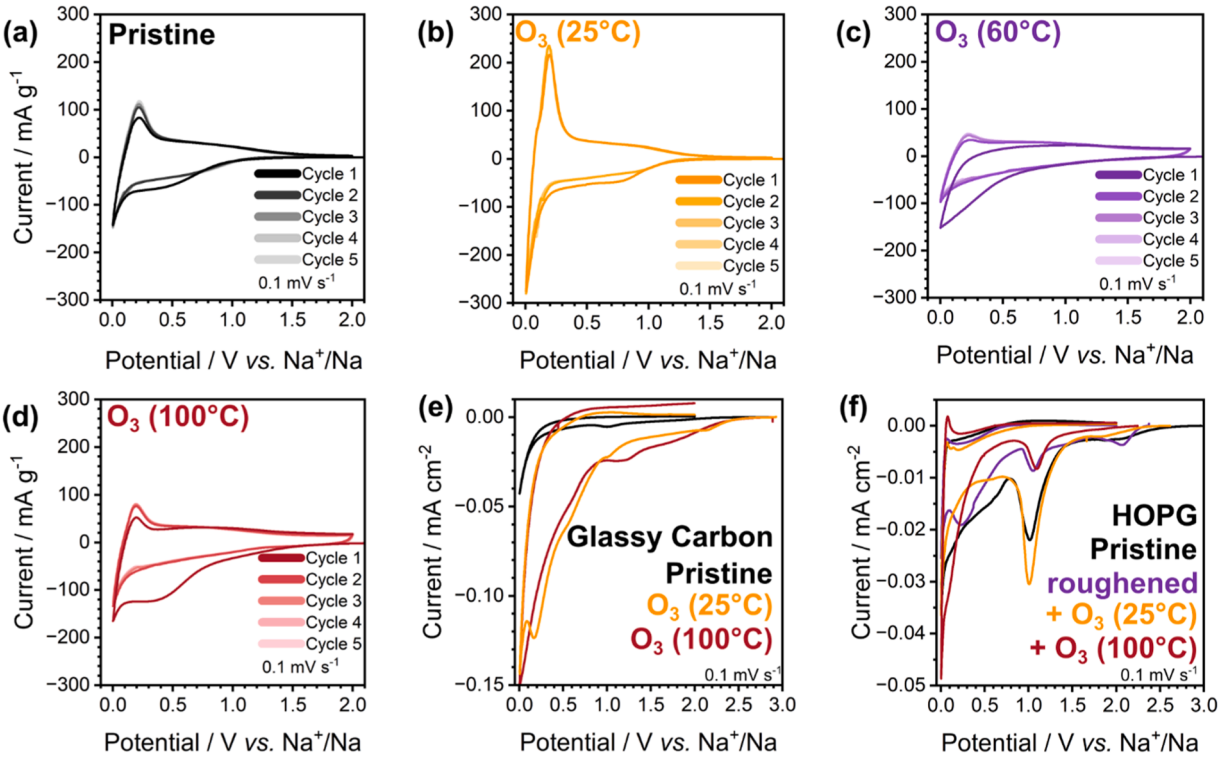

Fig. 6. (a-d) Cyclic voltammograms of the first five cycles of the hard carbon samples. (e,f) First-cycle cyclic voltammograms of pristine and ozone-treated GCE and HOPG electrodes. All measurements were performed between 2.0 V and 5 mV vs. Na^+/Na at 0.1 mV s^{-1}.

first-cycle cathodic currents below ~0.5 V vs. Na^+/Na, attributed to pronounced electrolyte decomposition and SEI formation (Fig. 6d). After treatment at 100 °C, LOCs are extensively fragmented and, in some regions, oxidized to such an extent that they have been released as CO_2, as evidenced by the observed mass loss. In HC–O3–60, however, LOCs remain immobilized within the particle. Moreover, in HC–O3–100, the severe oxidation and substantial material loss likely opened additional diffusion pathways, again enabling sodium storage within the porosity. HC–O3–100W closely resembles the profile of HC–O3–60, which agrees with the hypothesis that the LOCs may block the porosity, leading to diminished insertion currents (Fig. S9).

To further elucidate the effect of ozone functionalization, a b-value analysis based on the power-law $i = av^b$ was performed using cyclic voltammograms recorded at different scan rates (Fig. S10) [7–9]. The extracted b-values at 5 mV are significantly higher than those obtained at 0.4 V for all samples. At 0.4 V, b-values of approximately 0.4–0.5 indicate that sodium storage is predominantly diffusion-controlled within the sloping-potential region. In contrast, the higher b-values observed at 5 mV suggest an increased contribution from surface-controlled processes in the low-potential plateau region. Notably, HC–O3–25 exhibits the highest b-value at 5 mV, indicating facilitated sodium-storage kinetics in the plateau region, which is consistent with reports of mildly oxygen functionalized HC surfaces [9]. In contrast, HC–O3–60 and HC–O3–100 show substantially lower b-values at 5 mV, indicating a stronger contribution from diffusion limitation in the low-potential storage process. This behavior is consistent with the proposed formation of LOCs within the particle, which partially block the internal pore network and hinder Na^+ transport to low-potential storage sites. At 0.4 V, however, the b-values of HC–O3–60 and HC–O3–100 remain comparable to those of pristine HC, suggesting that ozone-induced LOC formation predominantly affects pore-filling processes in the plateau region while having only a minor influence on sodium storage in the sloping-potential region. Current separation according to $i(V) = k_1v + k_2v^{1/2}$ further corroborates these findings (Fig. S11). For all samples, the capacitive contribution increases with scan rate but remains below 80% even at 1 mV s^{-1}, demonstrating that sodium storage is not dominated by purely surface-controlled processes. HC–O3–25 exhibits a slightly higher capacitive contribution than pristine HC, whereas HC–O3–60 and HC–O3–100 show no substantial increase, consistent with the persistence of diffusion-limited sodium storage.

To decouple surface from bulk sodium storage effects, GCE and HOPG were examined as model substrates. First-cycle CVs of pristine and ozone-treated GCEs are compared in Fig. 6e. Pristine GCE shows low currents, consistent with negligible porosity and low surface polarity, and lacks a distinct anodic de-insertion peak, indicating predominantly irreversible electrolyte decomposition. After ozone treatment at 25 °C, the cathodic onset shifts to higher potentials (~2.0 V), signaling earlier interfacial reactions associated with sodium interaction with OFGs. A cathodic feature at ~0.2 V appears only for the ozone treated GCEs and is attributed to OFG induced SEI formation. In contrast to pristine GCE, ozone-treated GCEs exhibit higher first-cycle currents due to increased surface polarity and improved ion transport. Increased low-potential currents persist in subsequent cycles for treated GCEs (Fig. S12). Freshly cleaved HOPG shows a distinct cathodic feature at ~1.2 V in the first cycle that vanishes thereafter (Fig. 6f), consistent with irreversible electrolyte decomposition on basal-plane carbon, commonly associated with PF_6^- decomposition and NaF-rich SEI formation [56]. Mechanically roughened HOPG however shows different reactivity, as reduction peaks at ~2.1 and ~0.4 V emerge, while the feature at ~1.2 V is less pronounced also in the following cycles (Fig. S13). Interestingly, ozone treatment at 25 °C leads to a significant increase in the reduction peak at ~1.0 V during the first anodic scan, whereas at 100 °C the intensity is comparable to the untreated electrode. However, for both ozone treated HOPG samples the reduction peaks at higher and lower potentials are absent.

3.4.2. *Impedance spectroscopy*

Electrochemical impedance spectroscopy (EIS) was performed after five cycles to probe SEI and interfacial properties. Nyquist plots of HC

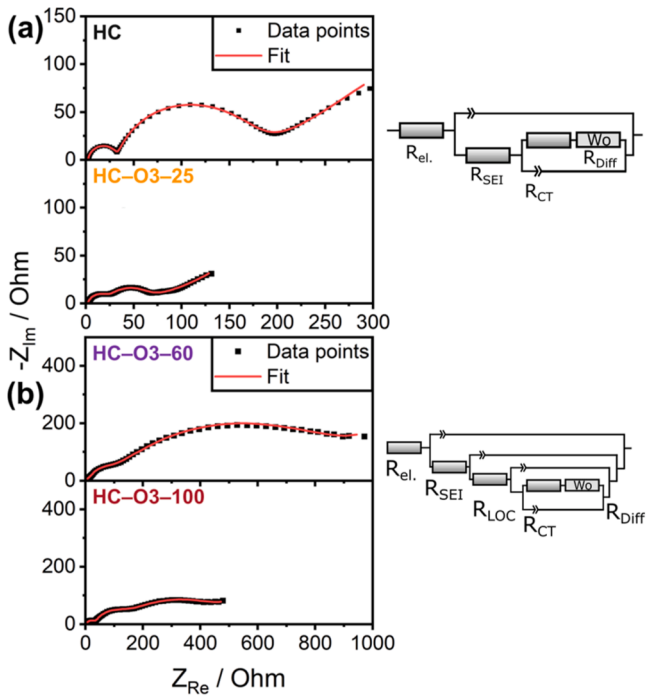

Fig. 7. Nyquist plots of pristine and ozone treated hard carbon after 5 formation cycles with corresponding equivalent circuits.

(Fig. 7a) comprise a high-frequency intercept corresponding to electrolyte resistance ($R_{electrolyte}$), a small high-frequency semicircle assigned to SEI resistance (R_{SEI}), a mid-frequency semicircle associated with charge-transfer resistance (R_{CT}), and a low-frequency Warburg-type tail reflecting sodium-ion diffusion in the porous carbon matrix [6]. A simplified Randles equivalent circuit was used to model the impedance spectra and to extract the relevant electrochemical parameters [57]. The nested structure of the equivalent circuit is well suited to approximate the impedance response of multi-particle electrodes and can be interpreted as a low-level analogue of a transmission line model. HC exhibits a R_{SEI} of 31 Ω, which decreases to 24 Ω for HC–O3–25 (Table 5). This reduction indicates a more ion-conductive SEI, consistent with favorable SEI formation induced by oxygen functionalization. A stronger effect is observed for R_{CT}, which decreases from 138 Ω (HC) to 33 Ω for HC–O3–25 (Fig. 7b), indicating facilitated Na^+ desolvation and interfacial transfer due to increased surface polarity and enhanced sodium-ion affinity of OFGs [5]

In contrast, HC–O3–60 and HC–O3–100 display an additional low-frequency semicircle (Fig. 7b), indicating an extra electrochemical process with a distinct time constant. To account for the LOCs generated by the ozone treatment, R_{LOC} was incorporated into the equivalent circuit as an additional RC element representing an ion-transport barrier. LOCs drastically increase the resistance of HC–O3–60, resulting in an additional R_{LOC} of 835 Ω. R_{SEI} (33 Ω) and R_{CT} (110 Ω) of HC–O3–100 are comparable to values from HC, while the resistive R_{LOC} fragments contribute an additional ~360 Ω, offsetting the beneficial effects observed for HC–O3–25. HC–O3–100W, on the other hand, shows a reduced R_{LOC} resistance of 159 Ω, further corroborating the negative impact of LOCs on the hard carbon (Fig. S14).

Overall, the EIS-derived reductions in R_{SEI} and R_{CT} for HC–O3–100 directly correlate with the enhanced insertion currents observed by CV, indicating improved interfacial kinetics. Conversely, the additional low-frequency process for HC–O3–60 and HC–O3–100 coincide with suppressed insertion behavior, reflecting kinetically hindered sodium transport due to LOCs.

Table 5
Overview of Samples and their calculated resistivities from charge transfer (R_{CT}), SEI (R_{SEI}) and LOCs (R_{LOC}).

Sample	R_{CT}	R_{SEI}	R_{LOC}
	/ Ω	/ Ω	/ Ω
HC	114	31	
HC–O3–25	33	24	
HC–O3–60	60	33	835
HC–O3–100	110	33	360
HC–O2–100	104	20	
HC–O3–100W	135	42	159

3.4.3. *Galvanostatic cycling*

Galvanostatic cycling at varying current densities and extended cycling was used to assess rate capability and long-term stability of ozone-treated hard carbon.

Rate performance is summarized in Fig. 8a. HC delivers an initial discharge capacity of ~190 mAh g^{-1}, which increases during the first cycles likely due to electrochemical activation, attributed to progressive access to previously inactive regions, potentially enabled by microcrack formation from local volume changes during sodiation [58]. In ozone-treated samples, this activation is not observed, consistent with ozone-induced pore opening and enhanced electrolyte accessibility already in the initial state.

Charge-transfer resistances originate at the SEI carbon interface and are governed primarily by ion desolvation energetics rather than SEI thickness, as established for Li-ion systems and can therefore reasonably be assumed for Na-ion systems [59]. In contrast, increased SEI thickness mainly raises ionic transport resistance across the interphase. This distinction is particularly relevant in the low-potential plateau region of hard carbon (<0.1 V vs. Na^+/Na), where diffusion-limited sodium insertion into pores dominates. Under these conditions, even small resistivity increases can significantly reduce accessible capacity, especially given the low cut-off potential (5 mV vs. Na^+/Na) employed to avoid sodium plating [60]. This diffusion-limited pore-insertion storage mechanism explains the impeded rate capability of HC–O3–60, as internal LOC formation blocks the porosity inside HC and conversely to HC–O3–100, they are not partly cleaved as CO_2.

At intermediate current densities (200 mA g^{-1}), the HC–O3–25 delivers the highest capacity, consistent with enhanced kinetics inferred from CV and EIS. At 1000 mA g^{-1}, capacities of all samples except HC–O3–60 converge to ~40 mAh g^{-1}, indicating that the applied current exceeds effective sodium diffusion through the SEI and carbon bulk. Although high-rate storage is sometimes attributed to surface processes, CV results show limited capacitive contribution and sodium insertion into the bulk remains operative but becomes diffusion-limited, analogous to fast-charging constraints in Li-ion batteries.

First-cycle voltage profiles (Fig. 8b) show the characteristic sloping region (1–0.1 V) followed by a low-potential plateau (<0.1 V) for HC, yielding an ICE of 74.9%. Ozone treatment at 25 °C shifts the onset of the sloping region to higher potentials, indicating earlier SEI formation, consistent with reports on functionalized hard carbons [6,54]. The slope-to-plateau capacity ratio increases markedly for the HC–O3–60 and HC–O3–100 (Table 6), which agrees with internal pore-blocking caused by LOCs. Furthermore, ICE drops to 44.7% (HC–O3–60) and 48.8% (HC–O3–100), reflecting extensive irreversible reactions with oxygen functional groups and LOCs. The oxygen-treated reference sample shows a profile similar to pristine hard carbon but with slightly reduced capacity and ICE (72.5%).

First-cycle differential capacity plots (Fig. 8c) further resolve potential-dependent processes complementary to CV. HC exhibits a sharp sodiation peak at ~0.03 V, corresponding to sodium storage in pores, in agreement with CV data. HC–O3–25 introduces an additional reduction peak at ~0.84 V, assigned to SEI formation, and enhances the low-potential peak near ~0.1 V, indicating more efficient pore filling. HC–O3–60 shows multiple reduction features (~0.7 V and ~0.48 V), evidencing sequential SEI formation and reactions with LOCs, while the

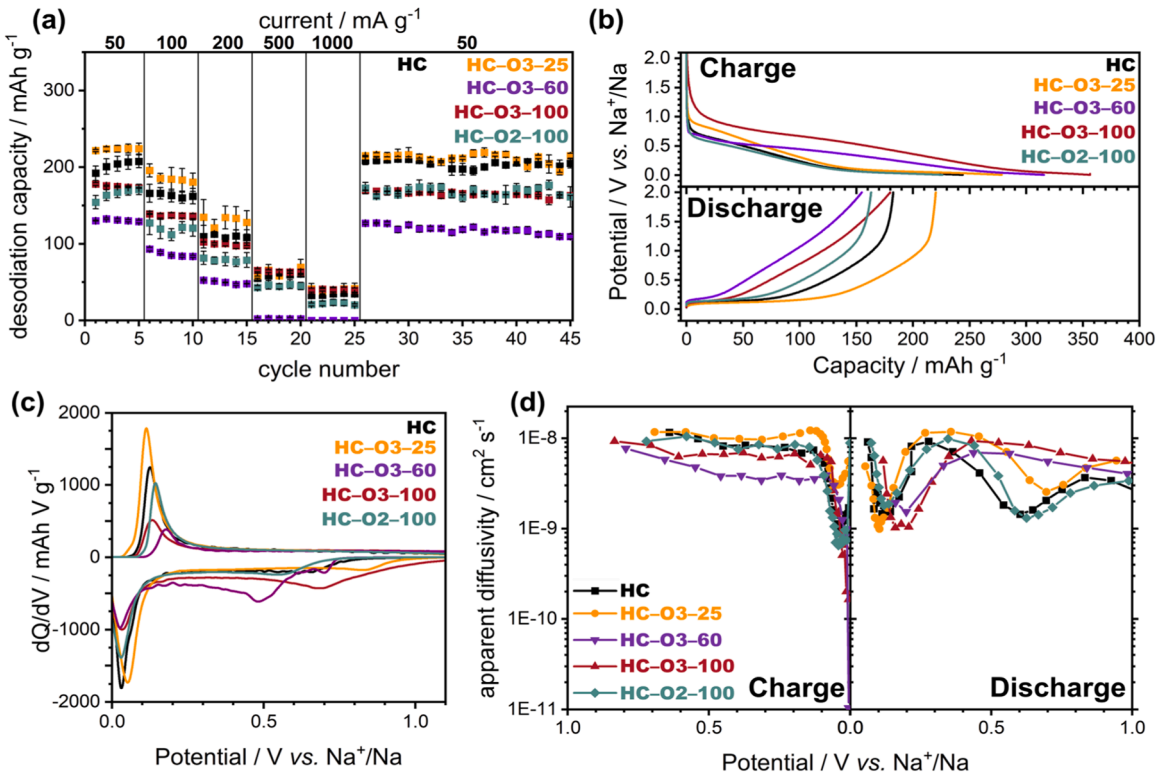

Fig. 8. (a) Rate performance of pristine and ozone-treated hard carbons measured between 2.0 V and 5 mV vs. Na^+/Na at current densities from 50 to 1000 mA g^{-1}. (b) First-cycle galvanostatic charge/discharge profiles at 50 mA g^{-1}. (c) Corresponding differential capacity (dQ/dV) plots. (d) Apparent sodium-ion diffusion coefficients determined by GITT after five formation cycles.

Table 6
Overview of Samples and Their Specific Capacities, Slopes, Plateau Capacities, and Initial Coulomb Efficiencies.

sample	reversible capacity at 50 mA g^{-1}	slope capacity	plateau capacity	slope / plateau ratio	initial coulombic efficiency
	/ mAh g^{-1}	/ mAh g^{-1}	/ mAh g^{-1}		/ %
Pristine	208	96	112	0.86	74.9
HC–O3–25	229	105	124	0.85	79.1
HC–O3–60	144	101	43	2.35	44.7
HC–O3–100	185	120	65	1.84	48.8
HC–O2–100	176	88	88	1.00	72.5

100 °C-treated sample displays a broader feature centered near ~0.7 V. These trends demonstrate that both the onset potential and complexity of SEI formation strongly depend on the nature and abundance of surface oxygen species and presence of LOCs.

Sodium-ion diffusion kinetics were analyzed by GITT after five formation cycles (Fig. 8d). The method follows the principle postulated by Weppner and Huggins, and the apparent diffusion coefficients were calculated using the equation reported by Bommier et al. as shown in Supplementary Fig. S15 [35,36]. HC–O3–25 exhibits significantly increased apparent diffusion coefficients at low potentials, indicating facilitated ion transport not only across the SEI but also within the particle. This supports the presence of functionalization within accessible internal porosity. As GITT yields effective diffusivities, these values also reflect interfacial and SEI contributions. In contrast, HC–O3–60 and HC–O3–100 markedly reduces apparent diffusivity at low potentials, consistent with over-functionalization and increased diffusion barriers due to LOCs blocking the internal porosity. Long-term cycling over 150 cycles at 50 mA g^{-1} (Fig. S16) revealed no additional degradation mechanisms beyond those already apparent from the first-cycle and rate-performance data. The relative capacity ranking of the samples remained unchanged throughout cycling, indicating that the effects of ozone treatment are established during the initial cycles and persist during prolonged operation.

4. Conclusion

This study demonstrates that ozone treatment exerts fundamentally different effects on hard carbon depending on the applied temperature. At 25 °C, ozone predominantly functionalizes the surface, whereas at elevated temperatures it acts as a molecular scissors, excising low-molecular highly-oxidized compounds from the carbon framework. Ozone treatment at 25 °C increases the surface oxygen content by ~15 at.% without evidence of subsurface oxidation, while higher treatment temperatures lead to oxygen contents of up to ~30 at.% and induce formation of LOC oxidation products inside the particles.

To rationalize these findings, a mechanistic framework based on a Criegee-type ozonolysis adapted to carbonaceous materials is proposed. Supported by spectroscopic evidence, the model identifies defects and edge sites as preferential reaction centers and explains how treatment conditions control both the nature and distribution of OFGs as well as the extent of structural degradation. This framework provides a consistent basis for linking ozone exposure conditions to surface chemistry and to the formation of LOC oxidation products.

The accessibility of the internal porosity emerges as the key factor controlling both ICE and reversible capacity, which stands in contrast to the widespread assumption that high surface oxygen content is the primary cause of low ICE. While ozone functionalization at 25 °C enhances ion-transport kinetics, as evidenced by reduced charge-transfer resistance, high-temperature ozone treatment promotes the formation of LOCs that obstruct internal pore networks, thereby reducing the reversible capacity of hard carbon.

Overall, these findings identify mild ozone treatment as a facile

functionalization strategy to introduce OFGs to the surface of hard carbon. Future work should focus on the selective introduction of specific OFGs to further optimize SEI formation and sodium-ion transport. This effort should be supported by advanced surface-sensitive characterization techniques capable of unambiguous identification of individual oxygen species.

CRediT authorship contribution statement

Felix Bauer: Writing – original draft, Visualization, Methodology, Investigation, Formal analysis, Data curation, Conceptualization. **Marius Ast:** Investigation, Formal analysis, Data curation. **Alperen Kahraman:** Data curation. **Frieder Scheiba:** Writing – review & editing, Supervision, Project administration, Funding acquisition.

Declaration of competing interest

The authors declare that they have no known competing financial interests or personal relationships that could have appeared to influence the work reported in this paper.

Acknowledgements

F. Bauer acknowledges T. Sostmann for conducting XRD measurements, A. Mathew and T. Nguyen for performing BET measurements, and V. Trouillet for assistance with XPS measurements. Special thanks are extended to M. Renner for invaluable discussions and support in the laboratory.

This work contributes to the research performed at CELEST (Center for Electrochemical Energy Storage Ulm-Karlsruhe) and was funded by the German Research Foundation (DFG) under Project ID 390874152 (POLiS Cluster of Excellence, EXC 2154).

Supplementary materials

Supplementary material associated with this article can be found, in the online version, at doi:10.1016/j.cartre.2026.100698.

Data availability

The data supporting this study are available at Zenodo under https://doi.org/10.5281/zenodo.20159084.

References

[1] M. Sawicki, L.L. Shaw, Advances and challenges of sodium ion batteries as post lithium ion batteries, RSC. Adv. 5 (2015) 53129–53154.
[2] P. Ge, M. Fouletier, Electrochemical intercalation of sodium in graphite, Solid State Ion. 28-30 (28–30) (1988) 1172–1175.
[3] M. Liu, J. Cai, Y. Zuo, W. Luo, Y. Huang, R. Qiu, Y. Luo, J. Lei, H. Yan, W. Yan, J. Zhang, Constructing continuously-distributed and crystalline-NaF-rich SEI on hard carbon anode through binder chemistry for high-performance sodium-ion batteries, Adv. Mater. 37 (2025) e05368.
[4] D. Sun, B. Luo, H. Wang, Y. Tang, X. Ji, L. Wang, Engineering the trap effect of residual oxygen atoms and defects in hard carbon anode towards high initial coulombic efficiency, Nano Energy 64 (2019) 103937.
[5] E. Olsson, G. Chai, M. Dove, Q. Cai, Adsorption and migration of alkali metals (Li, Na, and K) on pristine and defective graphene surfaces, Nanoscale 11 (2019) 5274–5284.
[6] F. Sun, H. Wang, Z. Qu, K. Wang, L. Wang, J. Gao, J. Gao, S. Liu, Y. Lu, Carboxyl-dominant oxygen rich carbon for improved sodium ion storage: synergistic enhancement of adsorption and intercalation mechanisms, Adv. Energy Mater. 11 (2021) 2002981.
[7] Y. Zhao, J. Ye, P. Zhang, Z. Li, H. Zhao, Abnormal preferential oxygen functionalization on the surface of soft/hard carbon for sodium storage, Appl. Surf. Sci. 602 (2022) 154336.
[8] W. Chen, C. Chen, X. Xiong, P. Hu, Z. Hao, Y. Huang, Coordination of surface-induced reaction and intercalation: toward a high-performance carbon anode for sodium-ion batteries, Adv. Sci. 4 (2017) 1600500.
[9] G. Zhao, X. Deng, Z. Wang, X. Wang, Boosting sodium storage performance of hard carbons by regulating surface oxygen functionalities, Mater. Lett. 396 (2025) 138783.
[10] C. Matei Ghimbeu, J. Górka, V. Simone, L. Simonin, S. Martinet, C. Vix-Guterl, Insights on the Na+ ion storage mechanism in hard carbon: discrimination between the porosity, surface functional groups and defects, Nano Energy 44 (2018) 327–335.
[11] L.A. Romero-Cano, H. García-Rosero, F. Carrasco-Marín, A.F. Pérez-Cadenas, L. V. González-Gutiérrez, A.I. Zárate-Guzmán, G. Ramos-Sánchez, Surface functionalization to abate the irreversible capacity of hard carbons derived from grapefruit peels for sodium-ion batteries, Electrochim. Acta. 326 (2019) 134973.
[12] H. Wang, F. Sun, Z. Qu, K. Wang, L. Wang, X. Pi, J. Gao, G. Zhao, Oxygen functional group modification of cellulose-derived hard carbon for enhanced sodium ion storage, ACS Sustain. Chem. Eng. 7 (2019) 18554–18565.
[13] Z. Wu, P.A. Webley, D. Zhao, Comprehensive study of pore evolution, mesostructural stability, and simultaneous surface functionalization of ordered mesoporous carbon (FDU-15) by wet oxidation as a promising adsorbent, Langmuir 26 (2010) 10277–10286.
[14] H. Zhao, J. Ye, W. Song, D. Zhao, M. Kang, H. Shen, Z. Li, Insights into the surface oxygen functional group-driven fast and stable sodium adsorption on carbon, ACS Appl. Mater. Interfaces 12 (2020) 6991–7000.
[15] W. Shao, F. Hu, T. Zhang, S. Liu, C. Song, N. Li, Z. Weng, J. Wang, X. Jian, Engineering ultramicroporous carbon with abundant C=oas extended 'slope-dominated' Sodium ion battery anodes, ACS Sustain. Chem. Eng. 9 (2021) 9727–9739.
[16] H. Xie, Z. Wu, Z. Wang, N. Qin, Y. Li, Y. Cao, Z. Lu, Solid electrolyte interface stabilization via surface oxygen species functionalization in hard carbon for superior performance sodium-ion batteries, J. Mater. Chem. A 8 (2020) 3606–3612.
[17] C. Shen, C. Wang, T. Jin, X. Zhang, L. Jiao, K. Xie, Tailoring the surface chemistry of hard carbon towards high-efficiency sodium ion storage, Nanoscale 14 (2022) 8959–8966.
[18] X. Li, G. Liu, B. Liu, P. Sun, Z. Wang, C. Wang, Z. Wang, F. Wu, H. Wang, Y. Cao, F. Zhang, Z. Mo, H. Cheng, D. Luo, G. Liu, Z. Lu, Oxygen plasma-treated hard carbon for high-rate and durable sodium-ion storage, ACS Appl. Mater. Interfaces 17 (2025) 46989–46997.
[19] Y. Zhu, M. Chen, Q. Li, C. Yuan, C. Wang, A porous biomass-derived anode for high-performance sodium-ion batteries, Carbon 129 (2018) 695–701.
[20] G. Lota, P. Krawczyk, K. Lota, A. Sierczyńska, Ł. Kolanowski, M. Baraniak, T. Buchwald, The application of activated carbon modified by ozone treatment for energy storage, J. Solid. State Electrochem. 20 (2016) 2857–2864.
[21] Y. Mulyana, M. Uenuma, Y. Ishikawa, Y. Uraoka, Reversible oxidation of graphene through ultraviolet/ozone treatment and its nonthermal reduction through ultraviolet irradiation, J. Phys. Chem. C 118 (2014) 27372–27381.
[22] F. Yang, M. Zhao, Z. Wang, H. Ji, B. Zheng, D. Xiao, L. Wu, Y. Guo, The role of ozone in the ozonation process of graphene oxide: oxidation or decomposition? RSC. Adv. 4 (2015) 58325–58328.
[23] P. Magne, N. Dupont-Pavlovsky, Graphite-ozone surface complexes, Carbon 26 (1988) 249–255.
[24] S.D. Razumovskii, V.N. Gorshenev, A.L. Kovarskii, A.M. Kuznetsov, A. N. Shchegolikhin, Carbon nanostructure reactivity: reactions of graphite powders with ozone, Fuller. Nanotub. Carbon Nanostructures 15 (2007) 53–63.
[25] K. Peng, L.-Q. Liu, H. Li, H. Meyer, Z. Zhang, Room temperature functionalization of carbon nanotubes using an ozone/water vapor mixture, Carbon 49 (2011) 70–76.
[26] P.P. Pal, T. Larionova, I.V. Anoshkin, H. Jiang, M. Nisula, A.A. Goryunkov, O. V. Tolochko, M. Karppinen, E.I. Kauppinen, A.G. Nasibulin, Dry functionalization and doping of single-walled carbon nanotubes by ozone, J. Phys. Chem. C 119 (2015) 27821–27828.
[27] T. Du, A.S. Adeleye, T. Zhang, N. Yang, R. Hao, Y. Li, W. Song, W. Chen, Effects of ozone and produced hydroxyl radicals on the transformation of graphene oxide in aqueous media, Env. Sci.: Nano. 6 (2019) 2484–2494.
[28] S. Groveman, J. Peng, B. Itin, I. Diallo, L.M. Pratt, A. Greer, E.J. Biddinger, S. G. Greenbaum, C.M. Drain, L. Francesconi, M. Vittadello, The role of ozone in the formation and structural evolution of graphene oxide obtained from nanographite, Carbon 122 (2017) 411–421.
[29] M.J. Webb, P. Palmgren, P. Pal, O. Karis, H. Grennberg, A simple method to produce almost perfect graphene on highly oriented pyrolytic graphite, Carbon 49 (2011) 3242–3249.
[30] W.-L. Yim, J.K. Johnson, Ozone oxidation of single walled carbon nanotubes from density functional theory, J. Phys. Chem. C 113 (2009) 17636–17642.
[31] J. Yao, H. Wang, J. Liu, K.-Y. Chan, L. Zhang, N. Xu, Preparation of colloidal microporous carbon spheres from furfuryl alcohol, Carbon 43 (2005) 1709–1715.
[32] J.H. Scofield, Hartree-Slater subshell photoionization cross-sections at 1254 and 1487 eV, J. Electron. Spectrosc. Relat. Phenom. 8 (1976) 129–137.
[33] A.V. Neimark, Y. Lin, P.I. Ravikovitch, M. Thommes, Quenched solid density functional theory and pore size analysis of micro-mesoporous carbons, Carbon 47 (2009) 1617–1628.
[34] D. Weingarth, M. Zeiger, N. Jäckel, M. Aslan, G. Feng, V. Presser, Graphitization as a universal tool to tailor the potential-dependent capacitance of carbon supercapacitors, Adv. Energy Mater. 4 (2014) 1400316.
[35] W. Weppner, R.A. Huggins, Determination of the kinetic parameters of mixed-conducting electrodes and application to the system Li3Sb, J. Electrochem. Soc. 124 (1977) 1569–1578.
[36] C. Bommier, T.W. Surta, M. Dolgos, X. Ji, New mechanistic insights on Na-ion storage in nongraphitizable carbon, Nano Lett. 15 (2015) 5888–5892.

[37] A.D. Delman, B.B. Simms, A.E. Ruff, On the mechanism of ozone degradation of SBR, J. Polym. Sci. 45 (1960) 415–434.
[38] J. Hoigné, H. Bader, The role of hydroxyl radical reactions in ozonation processes in aqueous solutions, Water Res. 10 (1976) 377–386.
[39] R. Blume, D. Rosenthal, J.-P. Tessonnier, H. Li, A. Knop-Gericke, R. Schlögl, Characterizing graphitic carbon with X-ray photoelectron spectroscopy: a step-by-step approach, Chem. Cat. Chem. 7 (2015) 2871–2881.
[40] Z. Ding, V. Trouillet, S. Dsoke, Are functional groups beneficial or harmful on the electrochemical performance of activated carbon electrodes? J. Electrochem. Soc. 166 (2019) A1004–A1014.
[41] D.J. Morgan, "Comments on the XPS Analysis of Carbon materials" *C* 2021, 7, 51.
[42] S. Kundu, Y. Wang, W. Xia, M. Muhler, Thermal stability and reducibility of oxygen-containing functional groups on multiwalled carbon nanotube surfaces: a quantitative high-resolution XPS and TPD/TPR study, J. Phys. Chem. C 112 (2008) 16869–16878.
[43] L. Li, X. Yao, H. Li, Z. Liu, W. Ma, X. Liang, Thermal stability of oxygen-containing functional groups on activated carbon surfaces in a Thermal oxidative environment, J. Chem. Eng. Jpn. 47 (2014) 21–27.
[44] J.C. Lascovich, R. Giorgi, S. Scaglione, Evaluation of the sp2/sp3 ratio in amorphous carbon structure by XPS and XAES, Appl. Surf. Sci. 47 (1991) 17–21.
[45] R. Criegee, Mechanism of ozonolysis, Angew. Chem. Int. Ed. Engl. 14 (1975) 745–752.
[46] S. Groveman, J. Peng, B. Itin, I. Diallo, L.M. Pratt, A. Greer, E.J. Biddinger, S. G. Greenbaum, C.M. Drain, L. Francesconi, M. Vittadello, The role of ozone in the formation and structural evolution of graphene oxide obtained from nanographite, Carbon 122 (2017) 411–421.
[47] S. Groveman, J. Peng, B. Itin, I. Diallo, L.M. Pratt, A. Greer, E.J. Biddinger, S. G. Greenbaum, C.M. Drain, L. Francesconi, M. Vittadello, The role of ozone in the formation and structural evolution of graphene oxide obtained from nanographite, Carbon 122 (2017) 411–421.
[48] F.J. López-Garzón, M. Domingo-García, M. Pérez-Mendoza, P.M. Alvarez, V. Gómez-Serrano, Textural and chemical surface modifications produced by some oxidation treatments of a glassy carbon, Langmuir 19 (2003) 2838–2844.
[49] A. Sadezky, H. Muckenhuber, H. Grothe, R. Niessner, U. Pöschl, Raman microspectroscopy of soot and related carbonaceous materials: spectral analysis and structural information, Carbon 43 (2005) 1731–1742.
[50] V. Meunier, A.G. Souza Filho, E.B. Barros, M.S. Dresselhaus, Physical properties of low-dimensional sp2-based carbon nanostructures, Rev. Mod. Phys. 88 (2016) 025005.
[51] D.B. Schuepfer, F. Badaczewski, J.M. Guerra-Castro, D.M. Hofmann, C. Heiliger, B. Smarsly, P.J. Klar, Assessing the structural properties of graphitic and non-graphitic carbons by Raman spectroscopy, Carbon 161 (2020) 359–372.
[52] F. Tuinstra, J.L. Koenig, Raman Spectrum of Graphite, J. Chem. Phys. 53 (1970) 1126–1130.
[53] A. Eckmann, A. Felten, A. Mishchenko, L. Britnell, R. Krupke, K.S. Novoselov, C. Casiraghi, Probing the nature of defects in graphene by raman spectroscopy, Nano Lett. 12 (2012) 3925–3930.
[54] M. Anji Reddy, M. Helen, A. Groß, M. Fichtner, H. Euchner, Insight into sodium insertion and the storage mechanism in hard carbon, ACS. Energy Lett. 3 (2018) 2851–2857.
[55] G. Hotová, V. Slovák, O.S.G.P. Soares, J.L. Figueiredo, M.F.R. Pereira, Oxygen surface groups analysis of carbonaceous samples pyrolysed at low temperature", Carbon 134 (2018) 255–263.
[56] M. Liu, F. Wu, Y. Gong, Y. Li, Y. Li, X. Feng, Q. Li, C. Wu, Y. Bai, Interfacial-catalysis-enabled layered and inorganic-rich SEI on hard carbon anodes in ester electrolytes for sodium-ion batteries, Adv. Mater. 35 (2023) 2300002.
[57] J.-M. Atebamba, J. Moskon, S. Pejovnik, M. Gaberscek, On the interpretation of measured impedance spectra of insertion cathodes for lithium-ion batteries, J. Electrochem. Soc. 157 (2010) A1218.
[58] K. Wang, Y. Xu, Y. Li, V. Dravid, J. Wu, Y. Huang, Sodium storage in hard carbon with curved graphene platelets as the basic structural units, J. Mater. Chem. A 7 (2019) 3327–3335.
[59] Y. Yamada, Y. Iriyama, T. Abe, Z. Ogumi, Kinetics of lithium ion transfer at the interface between graphite and liquid electrolytes: effects of solvent and surface film, Langmuir 25 (2009) 12766–12770.
[60] C. Müller, Z. Wang, A. Hofmann, P. Stueble, X. Liu-Théato, J. Klemens, A. Smith, Influences on reliable capacity measurements of hard carbon in highly loaded electrodes, Batter. Supercaps (2023).